**Supporting Information**

# Greatly-enhanced plasmon-exciton coupling in Si/$WS_2$/Au nanocavities

*Fu Deng[1#], Hongxin Huang[1#], Jing-Dong Chen[2], Shimei Liu[1], Huajian Pang[1], Xiaobing He[1], and Sheng Lan[1*]*

1. Guangdong Provincial Key Laboratory of Nanophotonic Functional Materials and Devices, School of Information and Optoelectronic Science and Engineering, South China Normal University, Guangzhou 510006, China

2. College of Physics and Information Engineering, Minnan Normal University, Zhangzhou 363000, China

[#] These authors contributed equally to this work.

*Corresponding Author: slan@scnu.edu.cn

## Supplementary Note 1: Comparison of Au/Au and Si/Au nanocavities (particle-on-film systems)

Previously, metallic nanoparticles and metallic particle-on-film systems have been employed to realize strong plasmon-exciton coupling. As compared with metallic nanoparticles, it is expected that the electric field can be further enhanced by using metallic particle-on-particle systems. For metallic particle-on-film sysytems constructed with spherical nanoparticles, it was found that the in-plane electric field is not enhanced so much although a large enhancement is achieved for the out-of-plane component. For this reason, metallic nanoprisms/nanocubes instead of nanospheres were generally used to construct all-metallic particle-on-film systems in order to achieve a large Rabi splitting. The situation is different when dielectric nanoparticle with large refractive indices are employed to creat dielectric-metal hybrid nanocavities (particle-on-film sysyems). In Figure S1, we present the in-plane electric field distributions calculated for Si/Au and Au/Au particle-on-film systems. The diameters of the Si and Au nanopsheres were chosen to be the same ($d$ = 172 nm). It is found that the in-plane electric field in the Si/Au nanocavity is much stronger when comparing with that in the Au/Au nanocavity, due mainly to the strong localization of the electrc field induced at the Fano resonance. In addition, it is noticed that the diameter of the ring-shaped electric field distribution in the Si/Au nanocavity is smaller than that in the Au/Au nanocavity.

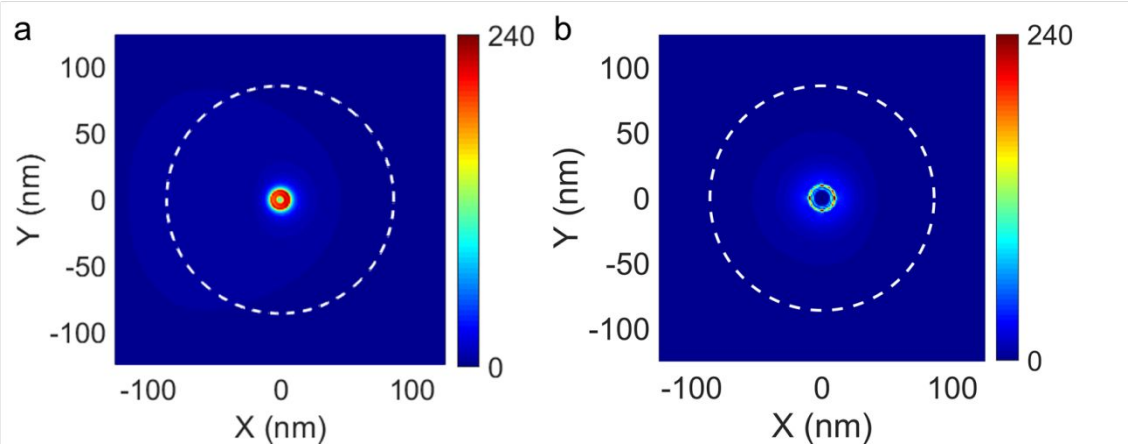


**Figure S1** In-plane electric field distributions calculated for (a) Si/Au and (b) Au/Au nanocavities created by using Si and Au nanospheres with the same diameter ($d$ = 172 nm) placed on a 50-nm-thick

Au film (or an Au/$SiO_2$ substrate).

## Supplementary Note 2: Experimental setup used for the measurements of angle-resolved scattering spectra

In Figure S2, we show the photo taken for the experimental setup used to measure the angle-resolved scattering spectra of Si/Au and Si/$WS_2$/Au nanocavities. The white light was coupled into a multimode optical fiber and collimated by using the combination of two optical lens so that a parallel white light was obtained. A polarizer was placed in front of the optical fiber to control the polarization angle of the white light. The whole system was fixed on an angle regulator so that the incident angle of the white light on the prism could be accurately adjusted.

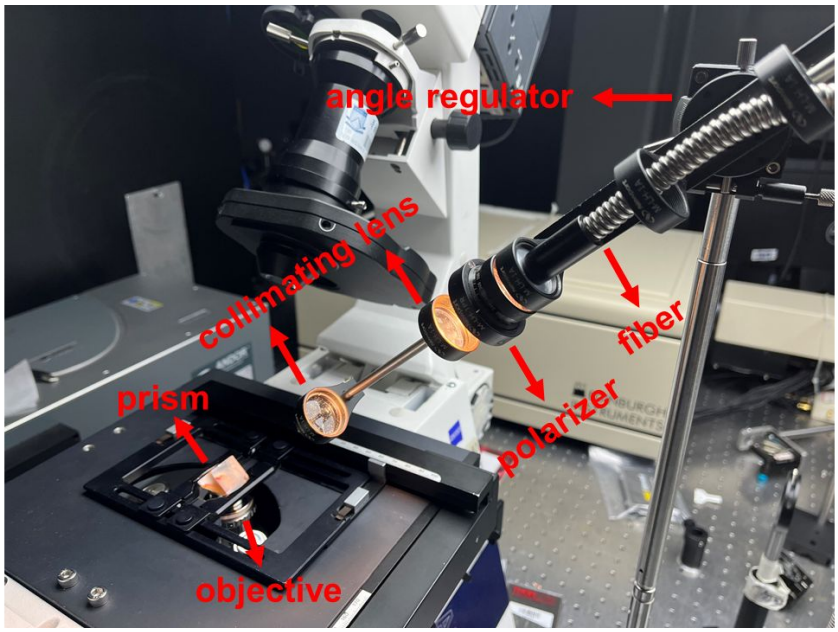


**Figure S2** Experimental setup used to measure the angle-resolved scattering spectra of Si/Au and Si/$WS_2$/Au nanocavities.

## Supplementary Note 3: Morphology and optical characterization of $WS_2$ monolayer

The $WS_2$ monolayers used in this work were firstly synthesized on a Si substrate by using chemical vapor deposition and then transferred to the $Au/SiO_2$ substrate. Figure S3a shows the bright-field images of triangular $WS_2$ monolayers on the thin Au film under a microscope. The scanning electron microscope (SEM) images of $WS_2$ monolayers are presented in Figure S3b. In order to characterize the quality of $WS_2$ monolayers, we measured the photoluminescence and Raman spectra of $WS_2$ monolayers and presented the typical spectra in Figure S3c,d. The photoluminescence peak of $WS_2$ monolayer was found at ~635 nm due to the Stokes shift. The monolayer nature of $WS_2$ flakes was confirmed by the Raman peaks revealed in the Raman spectra.

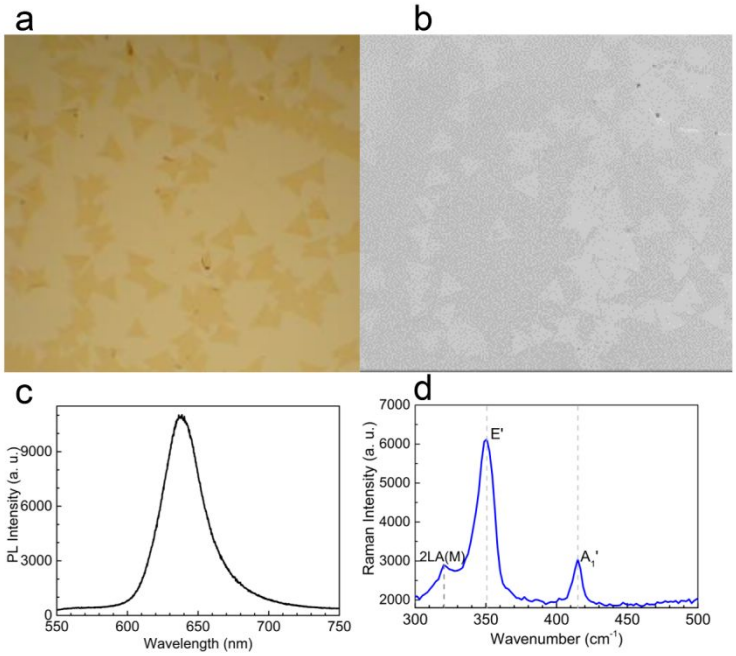


**Figure S3** Bright-field (a) and SEM (b) images of $WS_2$ monolayers on the $Au/SiO_2$ substrate. The typical photoluminescence and Raman spectra measured for $WS_2$ monolayers are shown in (c) and (d), respectively.

## Supplementary Note 4: Optical characterization of Si/Au and Si/$WS_2$/Au nanocavities

As described in the main text, Si/$WS_2$/Au nanocavities were created by dropping and drying the auqeous solution of Si nanoparticles on a $WS_2$ monolayer attached on the Au film. In Figure S4a, we show the bright-field image of $WS_2$ monolayers on which Si nanoparticles are randomly distributed. An enlarged image of a traiangular $WS_2$ monolayer is shown in Figure S4b, where a Si nanoparticle is enclosed by a dashed circle. In Figure S4c, we show the dark-field image of a $WS_2$ monolayer with attached Si nanoparticles, which was recorded by using illumination light with an incident angle smaller than the critical angle (i.e., $\theta < \theta_c$). The image of the same $WS_2$ monolayer obtained by using the SPPs generated on the Au film as the excitation source (i.e., $\theta > \theta_c$) is shown in Figure S4d. In this case, the scattering light intensity is greatly enhanced while a dark background is observed.

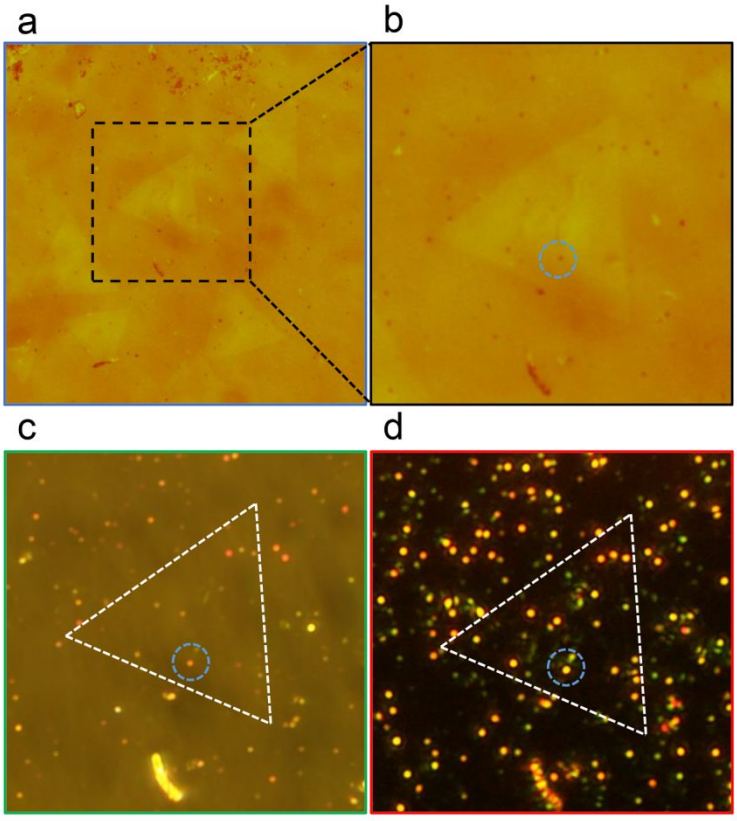

**Figure S4** (a) Bright-field images of $WS_2$ monolayers with attached Si nanoparticles. (b) The enlarged image of a $WS_2$ monolayer shown in (a). (c) Dark-field image of a $WS_2$ monolayer with attached Si nanoparticles obtained by using incident light with $\theta < \theta_c$. (d) Dark-field image of the same $WS_2$ monolayer shown in (c) excited by using the SPPs generated on the Au film (i.e., $\theta > \theta_c$). In both cases, the edge of the triagular $WS_2$ monolayer is marked by dashed lines and a typical Si nanoparticle on it is enclosed by a dashed circle.

## Supplementary Note 5: Optical properties of Si/Au nanocavities

As described in the main text, a Fano resonance is created in the scattering spectrum of a Si/Au nanocavity when it is ecxited by using the SPPs generated on the surface of the Au film. The Fano resonance is formed by the interference between the SPPs and the mirror-image-induced magnetic dipole (MMD), which originates from the coherent interaction of the electric dipole and its mirror image induced by the Au film. A typical example is shown in Figure S5a, where the scattering spectrum of a Si/Au nanocavity ($d$ = 169 nm) is presented. The angle of the incident light is chosen to be 45°. One can identify two scattering peaks (demoted as (1) and (3)) and one scattering valley (denoted as (2)). The electric field distributions in the xz plane calculated at the scattering peaks and valley are shown in Figure S5b.

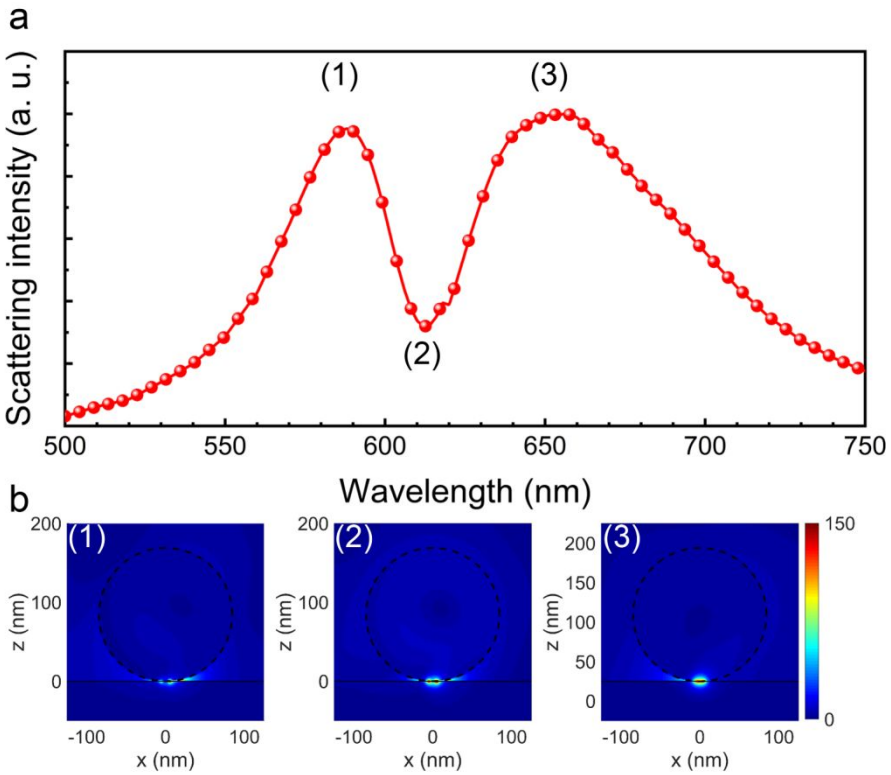

**Figure S5** (a) Scattering spectrum simulated for a Si/Au nanocavity composed of a Si nanoparticle with $d$ = 169 nm. (b) The electric field distributions in the xz plane calculated at the scattering peaks and the valley.

## Supplementary Note 6: Differences between Si/Au and Si/$WS_2$/Au nanocavities

As discussed in the main text, the Fano lineshape of the Si/Au nanocavity can be modified by simply varying the incidence angle. Now we compare the in-plane electric field distribution, which is crucial for plasmon-exciton coupling, calculated for Si/Au and Si/$WS_2$/Au nanocavities composed of Si nanoparticles with the same diameter ($d$ = 172 nm) at the Fano dip, as shown in Figure S6a,b. It is noticed that a ring-shaped intensity distribution is observed in both cases. However, the enhancement factor in the Si/Au nanocavity (~240) is much larger than that in the Si/$WS_2$/Au nanocavity (~35). In addition, the intensity distribution in the former is almost symmetric with respect to the y axis while an asymmetric intensity distribution is observed in the latter. We also examine the dependence of the enhancement factor on the incidence angle, which influences the Fano lineshape. The results are shown in Figure S6c,d. In the Si/Au nanocavity, the largest enhancement factor is found at 44.5°. In comparison, the largest enhancement factor is observed at 45° for the Si/$WS_2$/Au nanocavity.

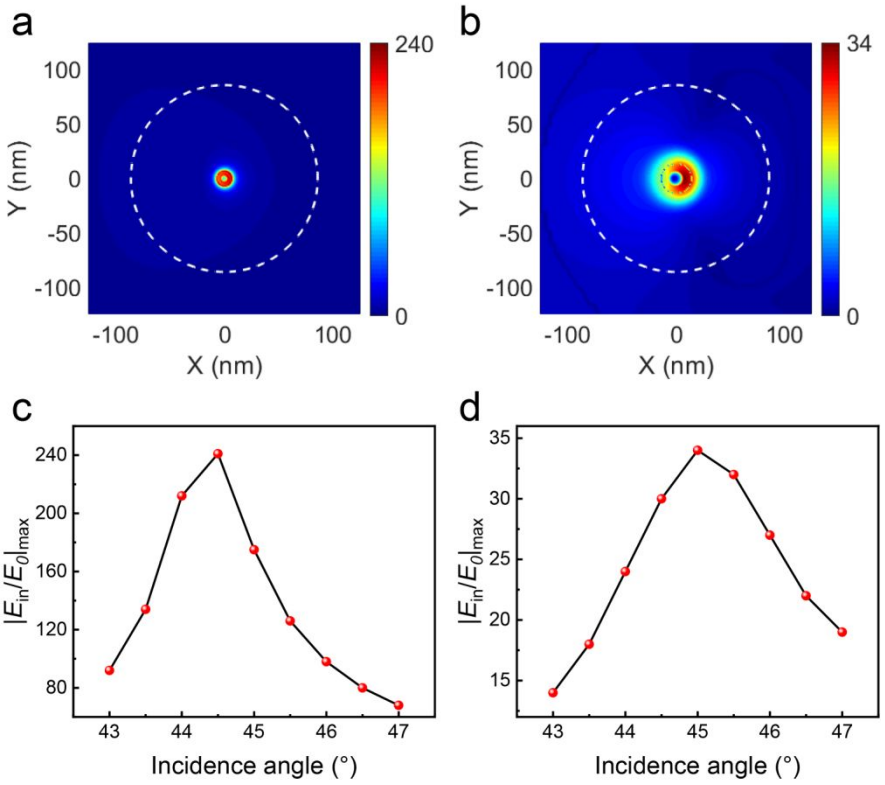


**Figure S6** In-plane electric field intensity distribution calculated for a Si/Au nanocavity (a) and a Si/$WS_2$/Au nanocavity (b) composed of Si nanoparticles with the same diameter ($d$ = 172 nm). The dependence of the enhancement factor on the incidence angle derived for the two nanocavities are shown in (c) and (d), respectively.

**Supplementary Note 7: Angle-resolved absorption spectra of the Si/$WS_2$/Au nanocavity**

In order to confirm that the scattering dips observed in the scattering spectra are really induced by the plasmon-exciton coupling rather than the absorption of the excitons, we also examined the angle-resolved absorption spectra of the Si/$WS_2$/Au nanocavity ($d$ = 172 nm), as shown in Figure S7. It is noticed that the angle-resolved absorption spectra are quite similar to the angle-resolved scattering spectra, indicating that the energy splitting is induced by plasmon-exciton coupling.

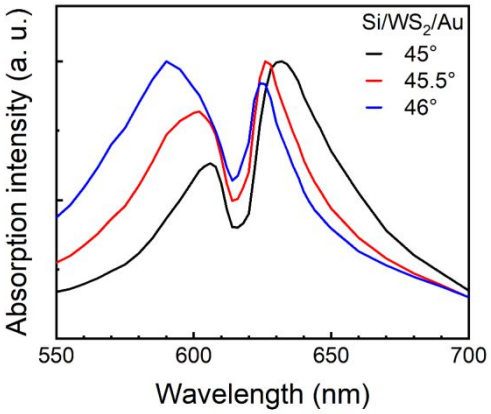


**Figure S7** Angle-resolved absorption spectra calculated for the Si/$WS_2$/Au nanocavity with $d$ = 172 nm.

## Supplementary Note 8: Comparison of plasmon-exciton coupling in different nanocavities coupled with TMDC monolayer

In Table I, we summarized the plasmon-exciton coupling realized in different nanocavities with an embedded TMDC monolayer reported in literatures. It is noticed that $WS_2$ and $WSe_2$ monolayers are commonly used in the study of plasmon-exciton coupling. The strong plasmon-exciton coupling was demonstrated by using either metallic nanoparticles or metallic particle-on-film systems. For dielectric nanoparticles, the photon-exciton coupling can only approach the strong coupling regime. It is found that the largest Rabi splitting was achieved by using Ag nanoprisms (120–150meV) and Au nanoprism-on-Au mirror systems (163 meV).

**Table I** Plasmon-exciton coupling in different nanocavities coupled with TMDC monolayers

| 2D materials | Resonator | T | Rabi splitting (meV) | Ref. |
|---|---|---|---|---|
| 1L $WS_2$ | Au nanorod | RT | 106 | 21 |
| 1L $WSe_2$ | Ag nanorod | RT | 49,5 | 22 |
| 1L $WS_2$ | Ag nanoprism | 6~300 K | 120-150 | 23 |
| 1L $WSe_2$ | Au bi-pyramids | RT | 83 | 25 |
| 1L $WS_2$ | Au nanodisk | RT | 108 | 26 |
| 1L $WS_2$ | Ag nanocube-Ag mirror | RT | 145 | 27 |
| 1L $WS_2$ | Au nanoprism-Au mirror | RT | 163 | 29 |
| 1L $WS_2$ | Si nanoparticle | RT | 110 | 34 |
| 1L $WS_2$ | Si nanosphere | RT | 43 | 35 |
| 1L $WS_2$ | Si nanosphere-Au mirror | RT | 72 | 38 |

| | | | | |
|---|---|---|---|---|
| 1L $WS_2$ | Ga nanosphere-Au mirror | RT | 120 | 39 |
| $WS_2$ nanodisk | — | RT | 190 | 45 |

RT, room temperature; L, layer.

## Supplementary Note 9: Mode hybridization in Si/Au and Si/$WS_2$/Au nanocavities

The strong coupling of the SPP, MMD, and exciton modes in a Si/$WS_2$/Au nanocavity leads to the formation of three hybrid states, which are referred to as upper, middle, and lower plexciton branches (UPB, MPB and LPB) based on their resonant energies. The fitting of the experimental data or the simulation results by using a Hamiltonian with three eigenvalues based on the coupled harmonic oscillator model, as we described in the main text, enables us to derive the Rabi splitting and the coupling strngthes between any of the two modes. In addition, the fraction of each mode in a mixed state can also be extracted. In Figure S9a, we show the dependences of the fractions of the SPP and MMD in the UPB and LPB on the resonant energy of the SPP derived for a Si/Au nanocavity with $d$ = 169 nm. Similarly, the dependences of fractions of the SPP, MMD, and exciton in the UPB, MPB, and LPB on the resonant energy of the SPP extracted for a Si/$WS_2$/Au nanocavity are shown in Figure S9b. For the Si/$WS_2$/Au nanocavity, it is noticed that the UP branch is mainly formed by the coupling of the SPP and the exciton and the contribution of the MMD is small. In addition, the MP branch is dominated mainly by the MMD and the exciton. Moreover, the LP branch is composed of the SPP and the MMD and contribution from the exciton is negligible.

For a two-oscillator system, it is well known that the criterion for strong coupling can be expressed as: $\Omega_{UP\text{-}LP} > (\gamma_1 + \gamma_2)/2$.[11] Similarly, the corresponding criterion for a three-oscillator system can be written as follows:[43]

$$\Omega > W_{UP}\gamma_{UP} + W_{MP}\gamma_{MP} + W_{LP}\gamma_{LP}, \quad \text{(S1)}$$

where $W_{UP}$, $W_{MP}$, and $W_{LP}$ are the weights of UP, MP, and LP branchs of the system, $\gamma_{UP}$, $\gamma_{MP}$, and $\gamma_{MP}$ are the linewidths of the three branchs. The weights for the three branchs can be derived by the following formula:

$$\begin{cases} W_{UP} = \gamma_{UP} / \left( \gamma_{UP} + \gamma_{MP} + \gamma_{LP} \right) \\ W_{MP} = \gamma_{MP} / \left( \gamma_{UP} + \gamma_{MP} + \gamma_{LP} \right) \\ W_{LP} = \gamma_{LP} / \left( \gamma_{UP} + \gamma_{MP} + \gamma_{LP} \right) \end{cases}. \tag{S2}$$

In addition, the linewidths of the three branches can be obtained brom the fractions of SPP, MMD and excitons modes in the hybrid states (see Figure S9b):

$$\begin{cases} \gamma_{UP} = 38\% \gamma_{SPP} + 25\% \gamma_{MMD} + 37\% \gamma_{ex} \\ \gamma_{MP} = 21\% \gamma_{SPP} + 18\% \gamma_{MMD} + 61\% \gamma_{ex} \\ \gamma_{LP} = 40\% \gamma_{SPP} + 59\% \gamma_{MMD} + 1\% \gamma_{ex} \end{cases}. \tag{S3}$$

By substituting Eqs. (S2) and (S3) into Eq. (S1), we can derive the criterion for the strong coupling of SPP-MMD-exciton modes as follows:

$$\Omega > 35\% \gamma_{SPP} + 37\% \gamma_{MMD} + 28\% \gamma_{ex}. \tag{S4}$$

In our case, we have $\Omega \approx 240$ meV, $\gamma_{SPP}$ = 220 meV, $\gamma_{MMD}$ = 89 meV, and $\gamma_{ex}$ = 33 meV. Apparently, the criterion for strong coupling is satisfied.

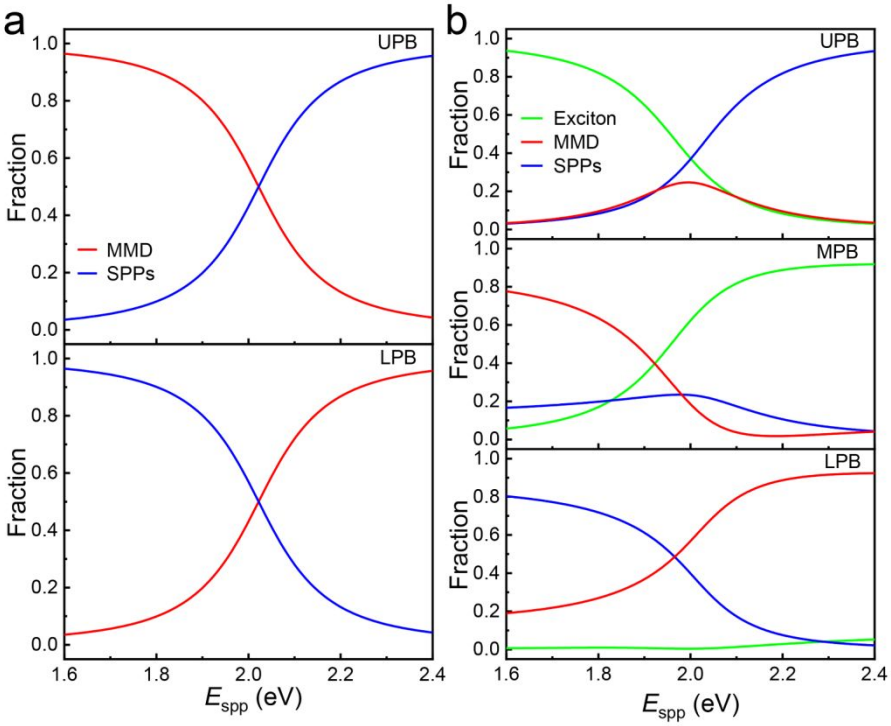

**Figure S9** (a) Dependences of the fractions of the SPP and MMD in the UPB and LPB on the resonant energy of the SPP derived for a Si/Au nanocavity with $d$ = 169 nm. (b) Dependences of fractions of the SPP, the MMD, and the exciton in the UPB, MPB, and LPB on the resonant energy of the SPP extracted for a Si/$WS_2$/Au nanocavity with $d$ = 172 nm.

## Supplementary Note 10: More experimental data for Si/$WS_2$/Au nanocavities

The experimental results for Si/Au and Si/$WS_2$/Au nanocavities described in the main text are typical examples. In experiments, we have measured the angle-resolved scattering spectra for many Si/$WS_2$/Au nanocavities, which are constructed by using Si nanoparticles with slightly different diameters, in order to characterize the enhanced plasmon-exciton coupling induced by the hybridization of the SPP, MMD, and exciton modes. In Figure S10a,b, we present the angle-resolved scattering spectra obtained for another two Si/$WS_2$/Au nanocavities composed of Si nanoparticles with sligly different diameters. In both cases, one can identify clearly two scattering dips (indicated by dashed lines) originating from the exciton and MMD resonances and three scattering peaks representing the resonant wavelengths of the three hybrid states. The difference in the diameter of the Si nanoparticle is reflected in the resonant wavelength of the MMD mode. In Figure S10c,d, we plot the resonant energies of the three hybrid states as a function of the resonant energy of the SPP, which are extracted from the angle-resolved scattering spectra shown in Figure 10a,b. In each case, the experimental data can be well fitted by using the coupled harmonic oscillator model with three oscillators (see solid curves in each case). The Rabi splitting energies are derived to be ~251 and 268 meV in the two cases, which are slightly larger than that observed in the Si/$WS_2$/Au nanocavity described in the main text.

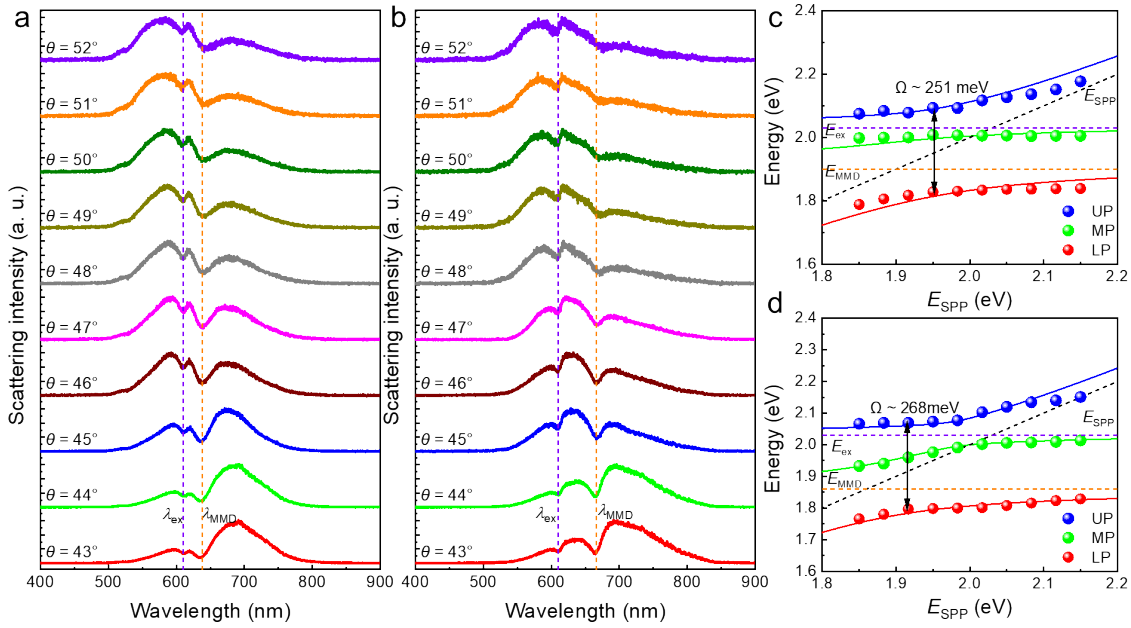

**Figure S10** Angle-resolved scattering spectra measured for Si/$WS_2$/Au nanocavities with (a) $d \sim 178$ nm and (b) $d \sim 189$ nm. The corresponding dependences of the resonant energies of the hybrid states on the resonant energy of the SPP extracted from the angle-resolved scattering spectra are shown in (c) and (d), respectively. The fitting results of the experimental data by using a coupled harmonic oscillator model with three oscillators are also shown.

## Supplementary Note 11: PL characterization of Si/$WS_2$/Au nanocavities

We have performed PL measurements for Si/$WS_2$/Au nanocavities that exhibit strong plasmon-exciton coupling. A typical example is shown in Figure S11, where the PL spectrum obtained for a Si/$WS_2$/Au nanocavity is compared with those obtained for the Au film, the $WS_2$ on the Au film ($WS_2$/Au), and an impurity nanoparticle (not Si nanoparticle) (impurity/$WS_2$/Au). It was found that the PL intensity from the Au film is much weaker than those from the $WS_2$/Au, impurity/$WS_2$/Au, and Si/$WS_2$/Au nanocavity. In addition, the PL intensity of the $WS_2$/Au is almost the same as that of impurity/$WS_2$/Au, implying that the modification of the local electric field due to the existence of the impurity is too small to introduce any change in the PL intensity. However, it is remarkable that the PL intensity of the Si/$WS_2$/Au nanocavity is reduced as compared with that of $WS_2$/Au or impurity/$WS_2$/Au. This phenomenon is quite similar to that observed in the PL characterization of metallic nanoparticles on a TMDC monolayer. In that case, an enhanced PL was observed in the weak and intermediate coupling regimes. In contrast, a reduction of PL was found in the strong coupling regime. Therefore, the reduction of the PL intensity observed for the Si/$WS_2$/Au nanocavity implies indirectly that the plasmon-exciton coupling has entered into the strong coupling regime.

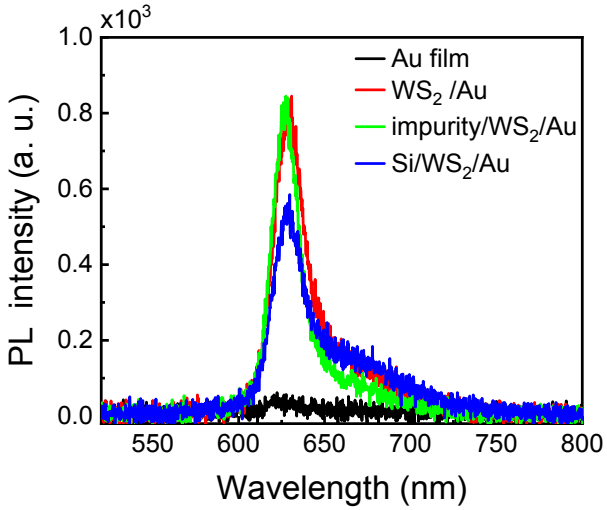


**Figure S11** PL spectra measured for a Si/$WS_2$/Au nanocavity which is resonant with the exciton in $WS_2$ monolayer. The PL spectra of the Au film, $WS_2$/Au, and impurity/$WS_2$/Au are also provided for comparison.